Exploration of geothermal systems using hyperspectral thermal infrared remote sensing

Kevin A. Reath *, Michael S. Ramsey

Department of Geology and Planetary Science, University of Pittsburgh, 4107 O'Hara Street, Pittsburgh, PA 15260, United States

ABSTRACT

Visible near infrared (VNIR), short-wave infrared (SWIR), and thermal infrared (TIR) remote sensing has long been used for geothermal exploration. Specific focus on the TIR region (8–12 μm) has resulted in major-rock-forming mineral classes being identified and their areal percentages to be more easily mapped due in part to the linear mixing behavior of TIR emission. To understand the mineral compositional and thermal distribution of active geothermal surfaces systems, hyperspectral TIR data from the Spatially Enhanced Broadband Array Spectrograph System (SEBASS) airborne sensor were acquired over the Salton Sea, CA geothermal fields by The Aerospace Corporation on March 26, 2009 and April 6, 2010. SEBASS collects 128 wavelength channels at ~1 m spatial resolution. Such high resolution data are rarely available for this type of scientific analysis and enabled the identification of rare mineral assemblages associated with the geothermally-active areas. One surface unit with a unique spectrum, believed to be a magnesium sulfate of unknown hydration state, was identified for the first time in the SEBASS data. The abundance and distribution of this mineral varied between 2009 and 2010 likely due to the precipitation conditions. Data obtained by the SEBASS sensor were also regressed to the 32 channel spectral resolution of the Mineral and Gas Identifier (MAGI) airborne sensor in order to test sensitivity limits. At this lower spectral resolution, all surface minerals were still effectively identified and therefore validated data at MAGI resolution are still very effective for accurate surface compositional mapping. A similar approach used at active geothermal areas in other semi-arid regions around the world has the potential to better characterize transient mineralogy, identify "indicators minerals", understand the influence of surface and ground water, and ultimately to locate new geothermal targets for future exploration. Furthermore, new Mineral and Gas Identification (MAGI) data serve as an excellent precursor for future spaceborne TIR data such as the system proposed for the Hyperspectral Infrared Imager (HyspIRI) instrument.

© 2013 Elsevier B.V. All rights reserved.

1. Introduction

1.1. Salton Sea geothermal area

The Salton Sea geothermal area (SSGA) is approximately 20 km^2 containing high heat flow, gryphons, and mud pots (Fig. 1A). It is bounded along the southeast margin by the Calipatria fault, which is an offshoot of the San Andreas fault (Younker et al, 1982). Currently, ten geothermal plants operate in the region to produce a combined capacity of 340 MW, enough energy to power over 100,000 homes. New geothermal fields have recently been exposed as the level of Salton Sea continues to drop with increasing water demands and less runoff. These new geothermal fields and surrounding regions have been the targets of energy exploration. Furthermore, the newly exposed shorelines have increased the potential of respiratory health impacts of the local population from the mineralogy of remobilized airborne dust.

The research presented here is focused on two locations within the SSGA. The first is the Davis–Schrimpf geothermal field (strip 1, Fig. 1B), which is a large, unvegetated field of mud pots and mud volcano-like gryphons located south of the geothermal plant, which is southeast of Mullet Island. Prior geologic and geothermal research has been conducted at this location (Ives, 1951; Helgeson, 1968; Elders et al., 1972; Van de Kamp, 1973; Elders and Sass, 1988; Herzig et al., 1988; Sturz et al., 1992; Svensen et al., 2007, 2009; Onderdonk et al., 2011; Lynch et al., 2013). The second location is an onshore geothermal field southeast of Mullet Island (strip 2, Fig. 1B) that was recently exposed due to lower water levels of the Salton Sea. The latter area is informally called the Sandbar geothermal field or the Morton Bay fumaroles; however for the purposes of this paper we will use the Sandbar nomenclature. For years, submarine fumaroles at this location were identified by water discoloration and increased water temperatures. Specific vent locations, geologic features, heat flow, and surface mineralogy can now be studied subaerially using airborne and ground-based TIR data.

Although the Salton Trough is composed mostly of shale at shallow depths (Herzig et al, 1988), the surface has become filled with quartz-
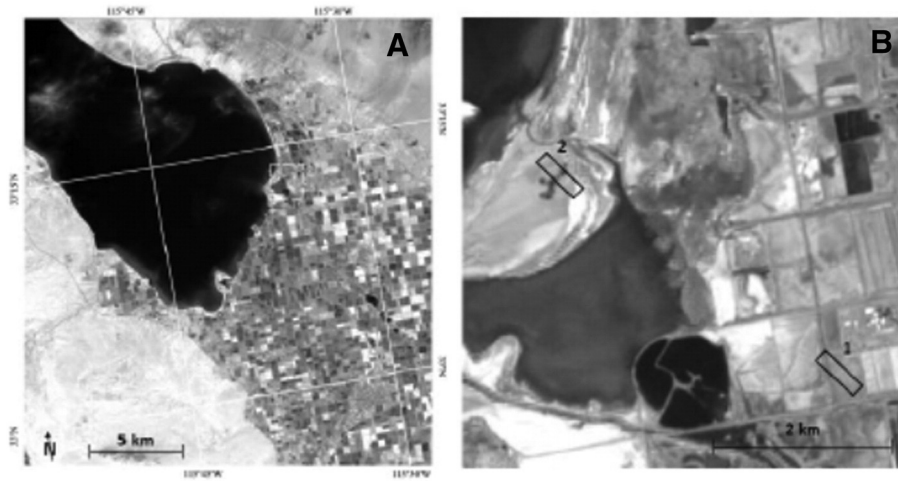
Fig. 1. ASTER VNIR (15 m pixel) image of the Salton Sea acquired on 9 October 2011 (A) Overview of the region with the white box indicating the area shown in B. (B) Detail of the field area with the location of the Davis–Schrimpf Geothermal Field (1) and the Sandbar Geothermal Field (2) shown by the black boxes.

rich sands and gravels derived from sandstone facies in the surrounding mountains. Local sources such as salt-based crusts near the retreating shore-line, silt/clay crusted sites, as well as regional ephemeral washes and distal alluvial fans (Buck et al., 2011; King et al., 2011; Sweeney et al., 2011) contribute to the geology as aeolian dust sources found in topographic depressions and to the salinity of the lake. In some areas evaporite minerals are also present. The mineralogy becomes more complex in areas surrounding active and formerly-active geothermal sites due to the brines that can contain up to ~25% Total Dissolved Solids (TDS) (Thompson and Fournier, 1988). In past analyses these brines were found to be of a unique composition, consisting heavily of sodium, potassium, calcium, and chlorine, with large amounts of iron, manganese, silica, strontium, boron, lithium, barium, lead, zinc, and copper (Helgeson, 1968).

Minerals containing these elements can easily be identified with TIR remote sensing and laboratory spectroscopy as long as the data have adequate spectral and spatial resolution and high signal-to-noise values. Therefore, geothermally active areas that produce enough energy to alter the local surface mineralogy should be easily identifiable remotely. We focus here on the accuracy, percentage, and distribution of such geothermally derived minerals at the SSGA.

1.2. Remote geothermal exploration

Over the last 40 years, remote sensing has been used for mineral detection and mapping (Short and Stuart, 1983; Gillespie et al., 1986; Hook et al., 2001). In that time, image processing techniques have also been developed to better identify and interpret rock and mineral signatures using TIR emissivity data (Kahle and Rowan, 1980; Gillespie et al., 1986; Ramsey and Christensen, 1998; Hook et al., 1999). However, thermal infrared remote sensing has been limited by past data quality, commonly with poor spatial and/or spectral resolution, and to a lesser extent, sensors with low signal to noise. Over time, the number of spectral channels has varied whereas the spatial resolution has continued to increase. For example, the Landsat Enhanced Thematic Mapper Plus (ETM+) instrument contained only one TIR channel at 60 m/pixel spatial resolution; the Advanced Spaceborne Thermal Emission and Reflection Radiometer (ASTER) has five TIR channels but at 90 m/pixel spatial resolution, whereas the new Thermal Infrared Sensor (TIRS) instrument on Landsat 8 contains only two channels at an even lower 100 m/pixel spatial resolution. Other sensors such as the Moderate Resolution Imaging Spectroradiometer (MODIS), the Advanced Very High Resolution Radiometer (AVHRR), and the Spinning Enhanced Visible and InfraRed

Imager (SEVIRI) each have between two and seven TIR channels, but at spatial resolutions of between 1.0 and 3.0 km/pixel. Multispectral instruments of ASTER/Landsat class have been most effective at broadly categorizing surface units (e.g., sulfates, carbonates, clays) than identifying specific minerals and their mixing components (Gillespie et al., 1984; Taranik, 1988; Sabine et al., 1994; Rowan et al., 2005; Zhang et al., 2007); whereas instruments of the MODIS class have been most effective at large-scale surface temperature mapping (Prata and Grant, 2001; Wright et al., 2002; Dean et al, 2004). By increasing the spectral resolution to 32 or 128 channels available with the MAGI and SEBASS sensors, respectively, distinct mineral types and suites can now be identified more accurately.

Much of this research presented here was performed in preparation for the first MAGI flight, which occurred in December 2011. This work served both as calibration/validation for the MAGI sensor, as well as a geologic study of the dynamic surface processes observed at the Salton Sea geothermal area. Results using data from MAGI are currently being analyzed and the manuscripts are in preparation.

1.3. Airborne TIR instruments

SEBASS is a hyperspectral airborne TIR pushbroom sensor designed and operated by The Aerospace Corporation (Hackwell et al, 1996). It has 128 channels in both the 2.5–5.2 μm and 7.5–13.5 μm spectral regions resulting in a spectral resolution of 0.088 μm (7 cm^{-1}) at 11.25 μm (890 cm^{-1}). The instantaneous field of view (IFOV) is 1.1 mrad and the total field of view (FOV) is approximately 7.3° (Vaughan et al., 2003). The instrument is commonly flown on a Twin Otter aircraft at an altitude of 915 m AGL resulting in ~1 m/pixel spatial resolution data with a swath width of 128 m in the cross-track direction and a signal-to-noise value of approximately 1000. Compared to the spaceborne ASTER TIR data, SEBASS data has sufficient spatial and spectral resolution to resolve all ground features and mineralogy found at the Davis–Schrimpf field. However, the total area covered by a single flight line of SEBASS is extremely narrow in comparison to other remote sensing instruments. For this study, SEBASS was flown over the SSGA and surrounding areas on 26 March 2009 and again on 6 April 2010. No coincident ground campaigns were conducted during these overflights, however ground data were later collected on March 2010 and June/July 2010 using the SEBASS data as a guide for specific mapping and sampling strategies.

The MAGI sensor has also been developed by The Aerospace Corporation to address technology development for the next generation of

spaceborne TIR sensors (Hall et al., 2008). It is a new 32 channel airborne TIR sensor with a spectral resolution 0.2 μm resulting in 32 spectral channels between 7.8 and 12.0 μm, a spatial resolution of 2 m/pixel at an altitude of 3657 m AGL, and a signal-to-noise value of approximately 500. It consists of a whiskbroom design that can acquire up to 2800 pixels in the cross track direction by compiling 128 pixel "whisks" in the downtrack direction (Hall et al., 2008). The number of whisks acquired is a function of the desired flight line length. This approach allows for a much wider crosstrack scan over multiple channels, which is a significant improvement over SEBASS. The sensor relies on a novel optical design, which incorporates a Dyson spectrometer that has small optical distortion at low f-numbers (dimensionless quantitative measurements of lens speed, Wolf and Born, 1965). This spectrometer is mated to a HgCdTe focal plane array that allows high frame rate data with very high signal to noise. The high spatial resolution and radiometric accuracy enables subtle spectral features, weak thermal anomalies, and weak gas-emission sources to all be detected (Hall et al, 2008). MAGI should allow more information to be obtained than earlier instruments while still collecting a majority of the data typical of more complex and costly hyperspectral sensors. The choice of 32 channels was made based on tests using SEBASS data with progressively degraded spectral resolution in order to determine the minimum number of channels that would still allow accurate mineral and gas discrimination. Because a majority of this work was completed prior to the first flight of the MAGI sensor, the SEBASS data were also degraded in spectral resolution to 32 channels (MAGI) and five channels (ASTER) for comparison and hypothesis validation.

2. Methods

2.1. ASTER data processing

In order to understand the long-term (seasonal to yearly) temperature variability of the SSGA, the ASTER TIR nighttime radiance data were examined. Nine cloud-free data scenes over seven years were chosen and the data ordered as atmospherically corrected surface radiance (Level 2, AST_09T product) (Abrams, 2000). These data were then separated into temperature and emissivity using the emissivity normalization approach (Gillespie, 1985; Realmuto, 1990). This process produces five emissivity images (one for each TIR channel) and one brightness temperature image for the 60 km^2 area covered within an ASTER scene. The thermal/temporal variations within the SSGA were determined by examining the nine temperature scenes. The emissivity data were also examined in order to assess any spatial or temporal differences in the surface compositional units.

2.2. SEBASS data processing

SEBASS TIR data are commonly delivered as radiance-at-sensor in "micro-flicks" units (μW/cm^2 ∗ sr ∗ μm). These data are first converted to W/m^2 ∗ sr ∗ μm units to allow for easy comparison to the ASTER temperature and emissivity products. The ENVI thermal atmospheric correction algorithm is a modified version of the in-scene atmospheric correction (ISAC) model developed by The Aerospace Corporation (Johnson and Young, 1998). This algorithm is necessary to remove the effects of atmospheric scattering and emission (Thome et al., 1998) and produce the radiance-at-ground data. Once the data were atmospherically-corrected, the emissivity normalization function was applied producing pixel-integrated brightness temperature and 128 channels of emissivity data.

2.3. Image deconvolution

The SEBASS data were explored for mineral/spectral variability in the Davis–Schrimpf geothermal field. A decorrelation stretch (DCS) was first applied to the 2009 radiance data, using channel 10

(8.20 μm), 25 (9.06 μm), and 69 (11.41 μm). This stretch displays variations in emissivity (i.e., composition) as color differences with temperature differences being displayed as variations in the color intensity (Gillespie, 1992a). The DCS is a quick and powerful visualization approach that is particularly effective for TIR data. Spectral variability between the color differences were compared to the actual SEBASS spectra and to laboratory emissivity spectra found both in the Arizona State University Thermal Emission Spectrometer (TES) spectral library (Christensen et al., 2000) and the ASTER spectral library (Baldridge et al., 2009). A common mineral suite/end member library was formed of the representative minerals found in the area by comparing spectral features found in the SEBASS data as well as incorporating minerals found in analogous regions located within or around the Salton Sea (Crowley and Hook, 1996; Onderdonk et al., 2011; Lynch et al, 2013). The end member suite consisted of quartz, gypsum, microcline, and anhydrite from the Arizona State University spectral library, as well as smectite and epsomite from the ASTER spectral library. Finally, using the using the pixel purity index (PPI) function in ENVI, a spectrum representing the unidentified hydrated Mg-sulfate mineral was identified in each SEBASS scene and incorporated into the end member suite.

The PPI function allows the pixels with the most unique spectra to be identified. These pixels will therefore contain the highest amount of a single spectral end member compared to any other pixel found in the scene. This process was only used to find the best Mg-sulfate mineral spectrum in both SEBASS scenes because of the instrument's high spectral resolution and the lack of a suitable example in any spectral library. Furthermore, the ease by which this mineral class can change hydration states, made it extremely difficult to locate in the field and transport to the laboratory spectrometer without altering its spectrum. The obvious weakness in the PPI approach to spectral extraction is that this spectrum still represents some amount of mixing within the pixel, which results in the PPI-based end member being overrepresented in the final deconvolution result. However, this error is greatly reduced with the high spatial and spectral resolution of the SEBASS data.

The final spectral end member suite was then applied to the SEBASS emissivity data using the linear deconvolution modeling approach of Ramsey and Christensen (1998). This approach produces a goodness-of-fit for the model and mineral maps of the surface that show the both the mineral constituents and percentages found in each pixel. The principle behind this approach is that emitted energy from a surface containing multiple end members combines linearly in the TIR and therefore can be deconvolved using a least-squares fit to a known set of mineral end members (Adams et al., 1986, 1989; Gillespie, 1992b; Ramsey and Christensen, 1998). In other words, the emitted energy from the different minerals is proportional to their aerial percentages within an image pixel.

Mineral maps using the selected end member suite were produced for the SEBASS, ASTER, and MAGI-simulated data. The end members were spectrally resampled prior to the deconvolution of each sensor's emissivity data. By definition, the deconvolution model is limited to a number of end members less than or equal to the spectral resolution of the data to be analyzed. Therefore, modeling of the ASTER emissivity data (five channels) was performed by running the deconvolution three times, each with different end member subsets. Both the 2009 and 2010 SEBASS scenes of the Davis–Schrimpf field were also analyzed using this approach. Three regions of interest were created for each year based on photogeologic interpretation of surface features and the linear deconvolution results.

2.4. Field methods

The SSGA was visited twice in 2010 (March and June/July). On each of these occasions verification and validation of the SEBASS data were performed. The area was thoroughly photographed and observed. During the March visit, which followed 1.3″ of rainfall (National Weather Service, 2011), the mudpots were observed to have formed large

pools around the gryphons. By July, this water had receded to several feet beneath the surface. Samples of mud from active gryphon slopes, liquefied mud within the gryphons, and soil surrounding the mudpots were collected. Surface samples were also collected in areas outside of the four active regions.

2.5. Lab methods

Several laboratory methods were employed to constrain the composition of the samples collected. TIR emission spectra of the samples were collected in the Image Visualization and Infrared Spectroscopy (IVIS) laboratory at the University of Pittsburgh using a Nicolet Nexus 670 FTIR spectrometer (Salisbury et al., 1994; Ruff et al., 1997; King et al., 2004). A full elemental SEM analysis was also performed on five grains of a sample believed to be the Mg-sulfate mineral that was collected in March. Once SEM analysis had identified elements found within the sample, XRD was used to identify specific minerals. The comparison of minerals in the XRD library was constrained to only those that contained elements found in the SEM analysis. Both the SEM and XRD analyses were performed at the Material Micro-Characterization Laboratory (MMCL) at the University of Pittsburgh.

3. Results

3.1. Mineral detection

The minerals chosen to create the spectral end member suite (Fig. 2) for the linear deconvolution process were based on similarity to the SEBASS emissivity spectra extracted from the March 2009 dataset (Fig. 3) as well as minerals reported in the area. The PPI function was used to extract the most "pure" image-based spectrum for the Mg-sulfate mineral in both the 2009 and 2010 SEBASS data. The spectra of these pixels (Fig. 4) were then included in the end member mineral suite. Mineral maps and the corresponding RMS error image were produced for both the 2009 (Fig. 5) and 2010 (Fig. 6) datasets. The lighter regions in the RMS image, which denote areas of higher error, were compared to each end member image to determine where areas of correlation and areas of spectral misfit occurred. Typical average errors of the linear deconvolution approach are on the order of ±2.5% for high spectral resolution data including laboratory and remote sensing sources (Ramsey and Christensen, 1998).

Detailed analysis of these mineral maps shows interesting results for both the mineral assemblages and their fractional abundances. Anhydrite ($CaSO_4$) appears to be underrepresented in these maps, which is likely due to the PPI end member spectrum containing some percentage of anhydrite in addition to the Mg-sulfate. In unmixing simulations not using the Mg-sulfate PPI spectrum, the area surrounding the geothermally active area becomes dominated by anhydrite. However, even with the Mg-sulfate PPI mineral included in the analysis, a large amount of anhydrite was still detected around the Davis–Schrimpf geothermal field (Fig. 7A). This same relationship also holds true for the Sandbar geothermal area (Fig. 8). Gypsum ($CaSO_4 \cdot 2H_2O$) can typically be found on the surface as a result of the evaporitic environment in the non-geothermally active, vegetation free zones (Herzig et al., 1988) (Fig. 7B). This suggests that in geothermally active areas, gypsum is being replaced by anhydrite due to dehydration from geothermal heating and/or surface heating in this arid environment. The spectrally-unique unit with features similar to the Mg-sulfate PPI spectrum was also detected surrounding the active vents. This spectrum has a strong absorption feature around 8.2 μm as well as a broad trough centered around 11.6 μm (Fig. 4), which are commonly found in sulfate minerals. It is this mineral that has been identified as a Mg-sulfate of an unknown hydration state (for reasons discussed in Section 4.1.2). As mentioned before, the area and percentages are somewhat over represented due to the likely inclusion of other minerals in the extract PPI spectrum (Figs. 5 and 6). However, the PPI spectrum is the most
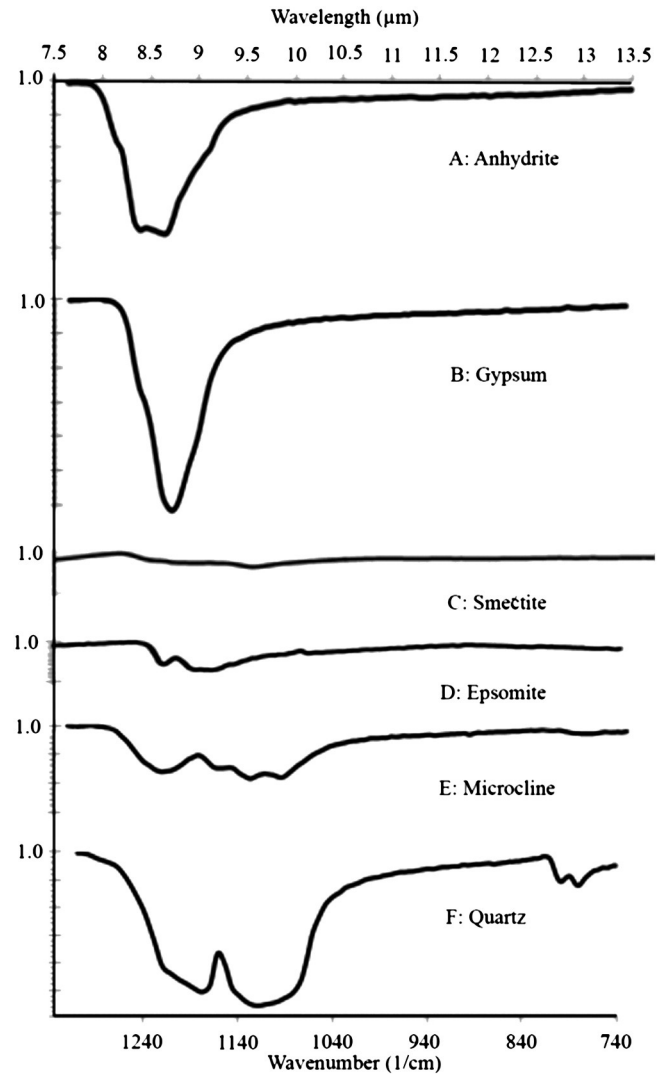
Fig. 2. Spectra of the mineral end member minerals used in the linear deconvolution process with a scale of 0.1 for the major tick marks and 0.01 for the minor tick marks.

spectrally-pure example of this mineral found in each SEBASS scene. All areas identified as containing this end member were also areas identified by the PPI making it likely that both models using entirely different approaches are finding the same mineral. This result also was found at the Sandbar geothermal field, where the same surface unit was identified surrounding the active vents. Much like the presence of anhydrite, this surface unit was only found surrounding the geothermally active areas in both the 2009 and 2010 SEBASS datasets.

The map of the Davis–Schrimpf field was divided into three regions based upon areal mineral diversity. The first region consists of the main vent area of the Davis–Schrimpf geothermal field and shows a wide variety of associated mineralogy including quartz, microcline, anhydrite, epsomite, and smectite. It is within this region that the majority of active geothermal activity at the site is found, its area increased from 1020 m^2 in 2009 to 2207 m^2 in 2010. The second region was identified as having a high percentage of the Mg-sulfate mineral. In 2009, this region covered approximately 5333 m^2; whereas in 2010, the area increased to approximately 15,895 m^2. Finally, the third region still contains a large percentage of the Mg-sulfate mineral, but also incorporates other minerals, such as anhydrite and quartz, which could be considered the typical background mineralogy in the area. It decreased from 24,027 m^2 in 2009 to 18,692 m^2 in 2010. The mineral maps for each of these regions were compared visually by placing the mineral
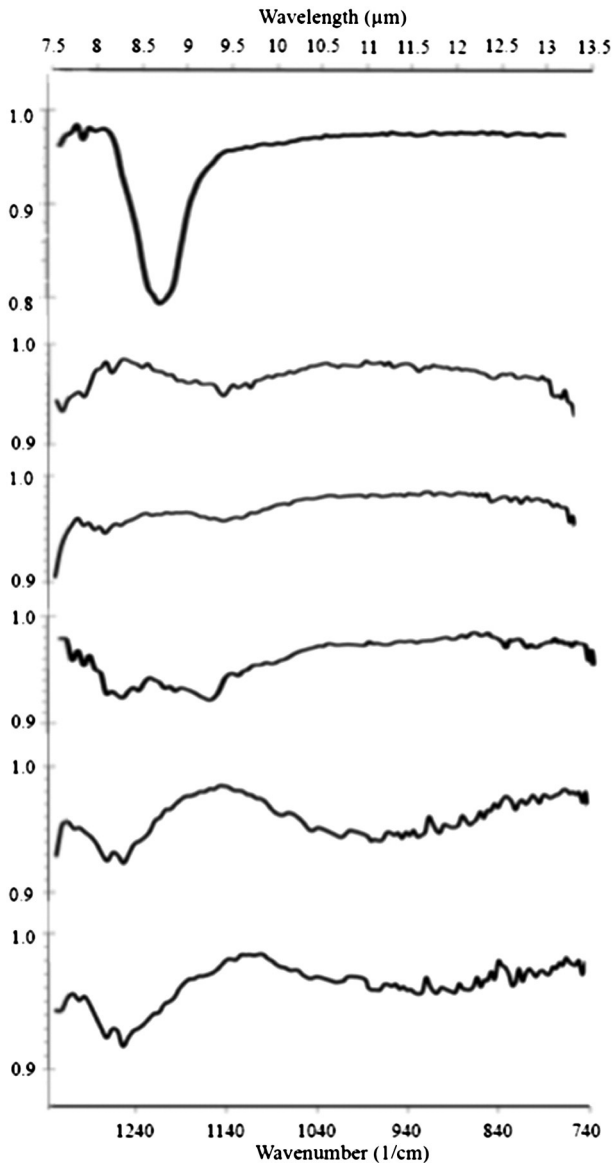
Fig. 3. Examples of SEBASS derived spectra found in the 26 March 2009 dataset with a scale of 0.1 for the major tick marks and 0.01 for the minor tick marks. Scemtite and epsomite spectra have been derived from the ASTER Spectral Library, quartz, microcline, anhydrite, and gypsum have been derived from the ASU TES spectral library.

Fig. 4. TIR spectra of the hydrated Mg sulfate mineral. The image-derived PPI spectra are shown for the 26 March 2009 and 6 April 6 2010 data, which were used in the deconvolution modeling. Note the TIR wavelength absorption feature at approximately 8.2 μm and the broader feature at longer wavelengths. The laboratory-derived spectrum of a sample collected in March 2010 is included for comparison.

end members in R, G, B, color composites as well as analytically by calculating end-member percentages of each region.

Identical regions of interest (ROIs) were chosen in the 2009 and 2010 scenes (Fig. 9). Changes in both the areal distribution of the mineral end members as well as the percentage of each end member were noted (Table 1). The most substantial difference was that of the area dominated by the spectrally-unique Mg-sulfate mineral. The areal coverage increased by almost 300% in less than a year. A slight increase in surface percentages was also noted where examining other end member difference between 2009 and 2010. This demonstrates that the deposits from 2009 have not merely been mechanically distributed over the surface through weathering, but rather, new deposits had formed on the surface between the 2009 and 2010 SEBASS overflights.

3.2. Spectral resolution effects

Emissivity data from ASTER and SEBASS (degraded to simulated MAGI) give an accurate representation of how the spectral resolution of these two sensors would affect the end member modeling and geologic interpretation. In order to study how spectral resolution alone would impact these interpretations, the spatial resolution and the signal-to-noise ratio were held constant at SEBASS values whereas spectral resolution was varied. As expected, a spectral resolution of five channels (ASTER) makes the accurate end member identification became extremely difficult. Furthermore, an increase in error was observed where comparing the full spectral resolution SEBASS to that of the emulated 32-channel MAGI (eMAGI), and the emulated 5-channel ASTER (eASTER) data. Only SEBASS and eMAGI data can be directly compared because the eASTER data does not have a sufficient number of TIR channels to support the analysis using the full seven end-member suite. However, four minerals at a time were used for the eASTER deconvolutions. This allowed for a basic understanding of how well these mineral can be identified with the TIR spectral resolution of ASTER (Fig. 9, Tables 2 and 3).

Both the SEBASS and eMAGI mineral maps are visually similar (Fig. 10). Areas identified as being rich in anhydrite and the Mg-sulfate mineral in SEBASS data were also found comparable to the same areas in eMAGI data (Tables 2 and 3). There were, however, some slight variations. For example, the eMAGI data assigned the Mg-sulfate mineral end member to slightly more areas and reduced the contrast between mineral rich areas. The percentage difference ranged from 0% to 12%, with the majority of that difference being below 2.5%.

In contrast, deconvolution of the eASTER scene produced very different results due to the significant loss of spectral resolution (Fig. 10). Anhydrite was positively identified in the eASTER data surrounding the geothermal field. However, anhydrite was also identified in every other surveyed area of the Salton Sea as well. The Mg-sulfate surface unit surrounding the geothermal vents was not detected at all and the RMS error was higher in all regions. The difference in percentage between the SEBASS and eASTER data range from 0 to 35% with several minerals having differences above 10% (Tables 2 and 3). In the eASTER data, pixels were also found to be generally more homogenous with a single end member dominating most pixels with percentages greater than 70%.
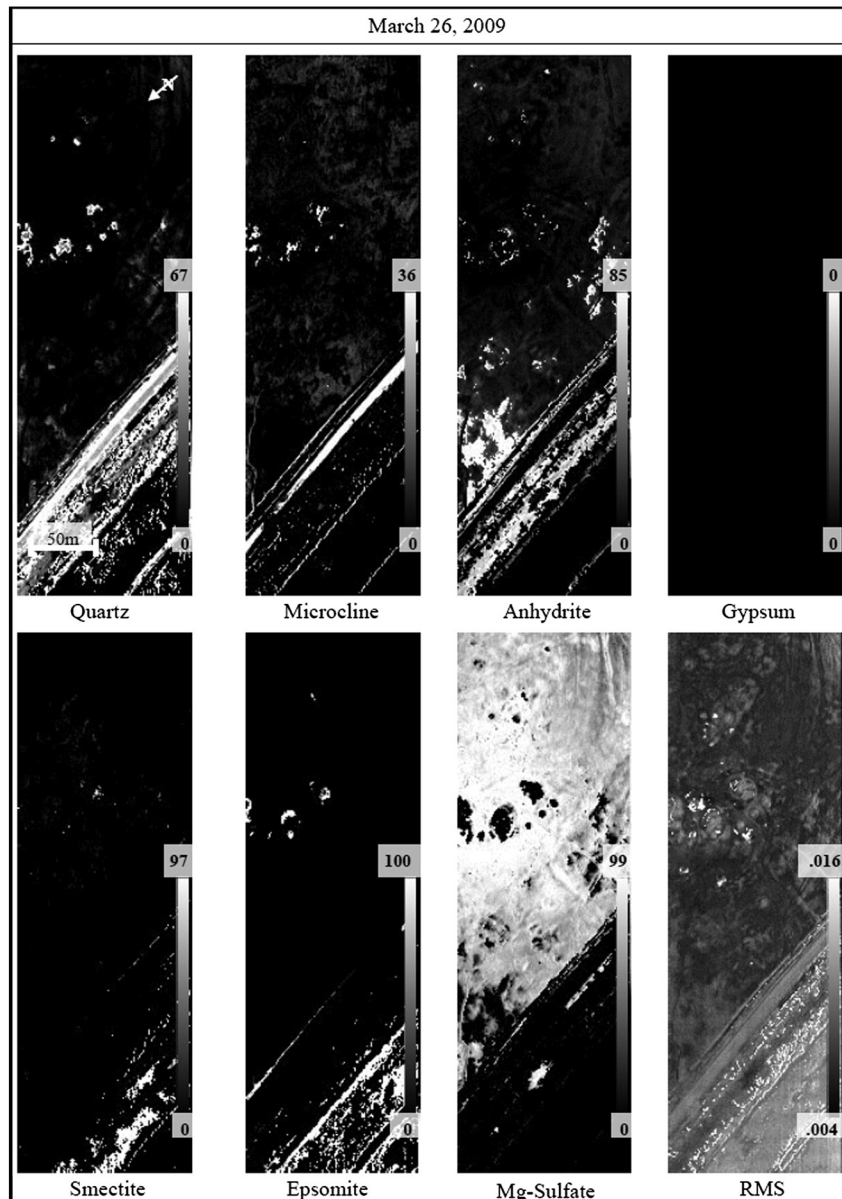
Fig. 5. Mineral maps of the Davis–Schrimpf geothermal field derived from the 26 March 2009 SEBASS data. The dynamic range is shown on the right of each image with the values corresponding to the mineral percentages. Anhydrite can also be found in large amounts surrounding the geothermal field, where as gypsum is not detectable in this area. The Mg sulfate map shows a concentration around the geothermal vents but is also somewhat overrepresented due to the PPI-derived end member spectrum being a mixture to start.

4. Discussion

4.1. Mineral detection

The surface mineralogy of several geothermal fields in the Salton Sea region was explored using TIR remote sensing and laboratory spectroscopy. The calibrated emission spectra were subjected to a linear deconvolution modeling approach and resulted in two important findings. The first was that anhydrite was located in close proximity to the geothermally active areas, whereas gypsum was found to be abundant throughout the region, but not directly surrounding these same geothermal areas. Second, a spectrally unique mineral that is likely a Mg-sulfate of an unknown hydration state, was identified in the TIR data. The spectrum of this mineral did not match and sulfate in current spectral libraries and much like the anhydrite, could only be found surrounding the geothermally active areas. To better represent this spectrally unique mineral, a pixel purity index was performed on the SEBASS data in order to locate the pixel containing the highest

percentage of this likely Mg-sulfate mineral. This spectrum was then used in the end member suite for linear deconvolution model.

4.1.1. Anhydrite/gypsum

The surface and subsurface conditions present at the SSGA favor formation of both gypsum and anhydrite (Helgeson, 1968). Gypsum has been mined in the region and in 1984 anhydrite was encountered in the Salton Sea Drilling Project (SSDP) borehole. This anhydrite was found in nodular textures, similar to those found in gypsum, therefore suggesting that anhydrite had replaced gypsum (Herzig et al., 1988). Furthermore, intrasediment growth of anhydrite nodules is a common feature of burial alteration of gypsum to anhydrite (Spencer, 2000). It has also been shown that where gypsum is hydrothermally heated to approximately 120 °C, a sharp transition occurs from fast growth to fast dissolution (Jordan and Astilleros, 2006). At this temperature, anhydrite is a more stable phase than gypsum. The Salton Sea geothermal system has been found to produce brines in excess of 350 °C at a depth of 1400 m (Elders and Sass, 1988), and therefore anhydrite is
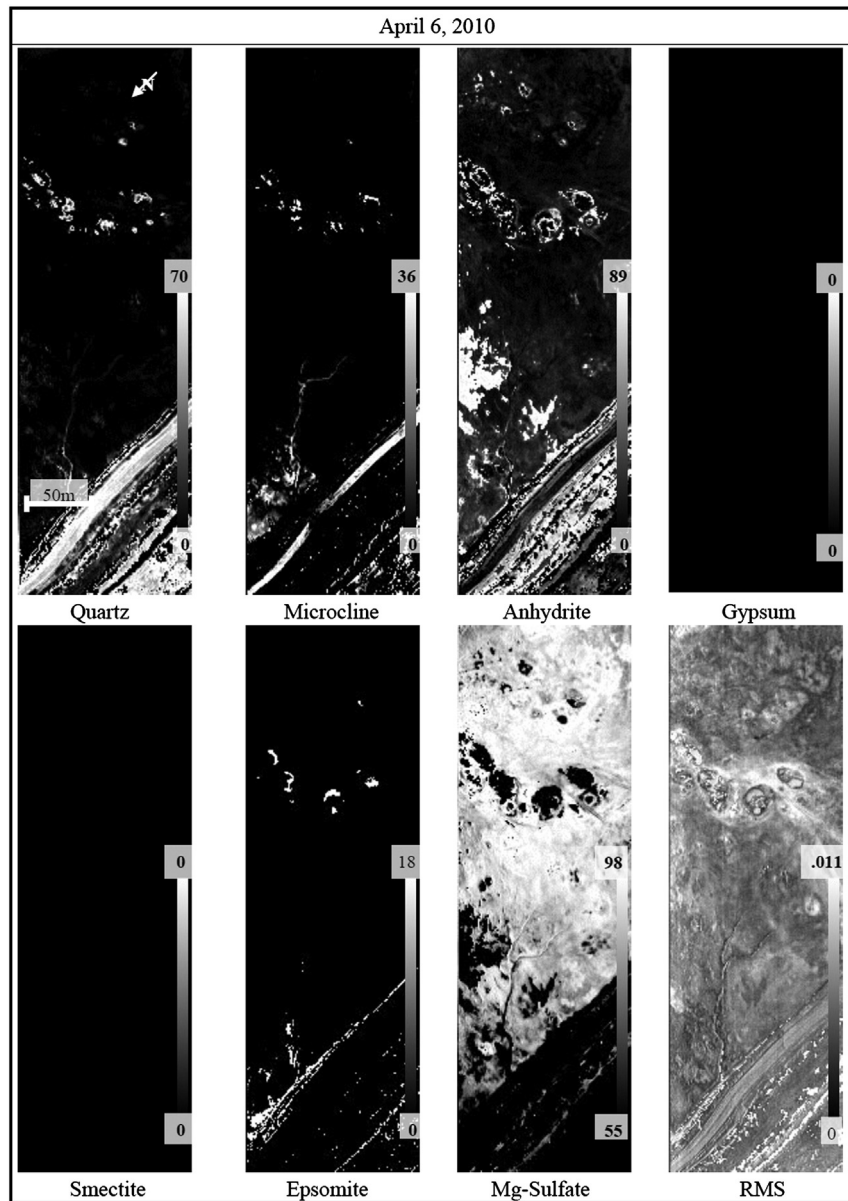
Fig. 6. Mineral maps of the Davis–Schrimpf geothermal field derived from the 6 April 2010 SEBASS data. As seen in the 2009 data, anhydrite can also be found in abundance, gypsum is not detectable, and the Mg sulfate could be somewhat overrepresented.

likely to be forming at depth in dry regions depending on the associate geochemical system. Because of the temperatures needed to create sub-surface anhydrite as well as the transport process needed to move the mineral to the surface, anhydrite appears to only be associated with the most geothermally active areas of the Salton Sea. Although in some areas, remnants of anhydrite were found in regions that could have potentially been active in recent history or are starting to develop enough geothermal heat to create anhydrite (Fig. 7C). Similarly, the Mg-sulfate mineral unit was found in the highest concentrations surround-ing geothermally active areas, although it is was well-distributed throughout the SEBASS scene. We therefore postulate that the increased heat at these vents help accelerate the transition of gypsum to anhydrite and accelerate the formation of the Mg-sulfate. Therefore, it is possible that the geothermal brines and liquefied mud transported anhydrite and the Mg-sulfate formed at depth to the surface and deposits them proximal to the vents.

Alternatively, anhydrite could also be leached out onto the surface following mixing with meteoric ground and surface waters (Azimi and Papangelakis, 2010). In the presence of pure water, at the typical surface pressure of 1 atm, gypsum is the stable phase for calcium sulfate for tem-peratures below 40 °C, anhydrite is the stable phase for higher tempera-tures (MacDonald, 1953). Both the seven year ASTER thermal profile of the region and field measurements taken in 2010 found maximum sur-face temperatures of 38 °C. Although these temperatures were not hot enough for anhydrite to form on the surface, the proximity of these tem-peratures to the gypsum–anhydrite transition and air temperatures that commonly exceed 40 °C in the summer months mean that anhydrite is likely to form on the surface in sabhka-style syndepositional surface al-teration. However, climate conditions throughout most of the year at the Salton Sea would favor gypsum rather than anhydrite and both over-flights took place in early spring when air temperatures were too cool for anhydrite formation. Therefore, any anhydrite found on the surface would likely have been deposited relatively recently before the over-flights or formed solely due to subsurface heat flow. If this process rely-ing only on air temperatures were the dominant formation mechanism however, we would expect to find widespread anhydrite throughout the region, which is not the case. Therefore, subsurface heat flow is clear-ly critical in the mineral's formation and stability on the surface.
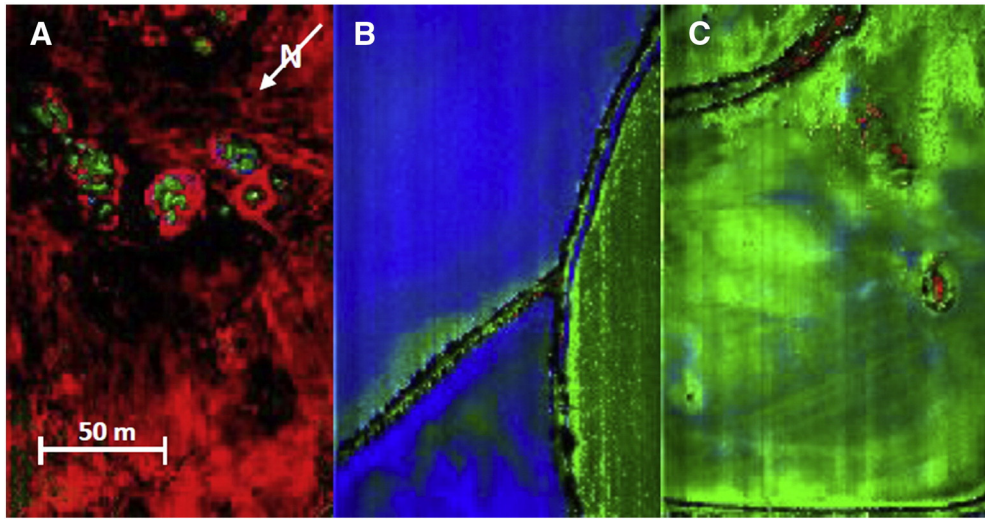
Fig. 7. End member mineral maps of three subscenes from the same SEBASS overpass collected on 6 April 2010 showing anhydrite in red, gypsum in blue, and quartz in green. A) Geothermal vents showing a larger concentration of anhydrite. B) Large amounts of gypsum identified on the surface of typical agricultural fields. C) Inactive geothermal vents can be identified by sparse amounts of anhydrite at the surface.
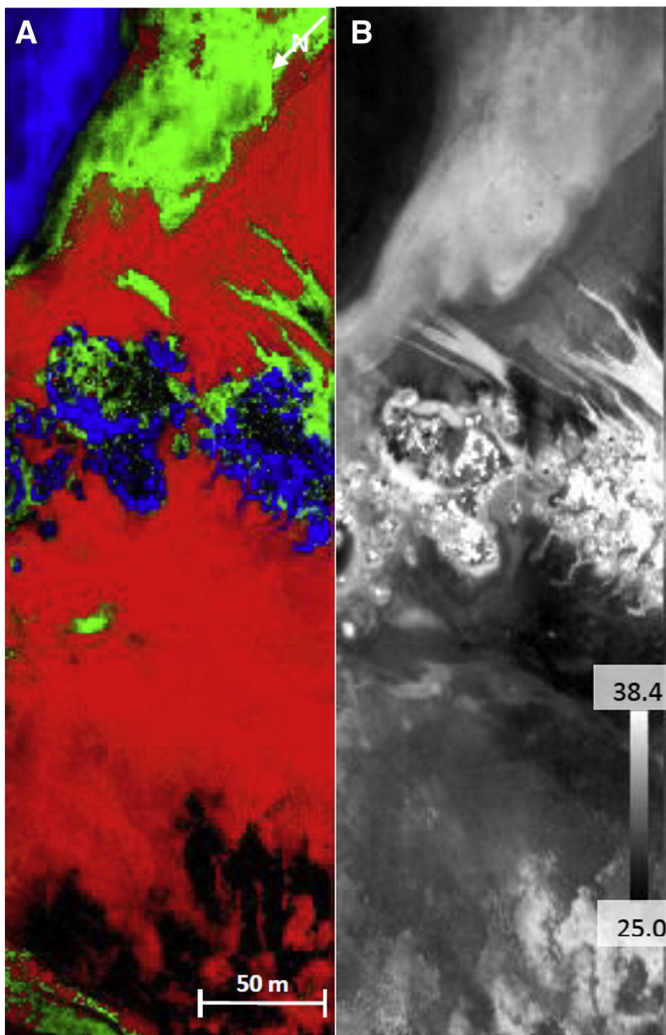
Fig. 8. SEBASS data of the Sandbar Geothermal field acquired on 6 April 2010. (A) Mg sulfate mineral in red, anhydrite in green, and gypsum in blue. Note the large amounts of both anhydrite and the Mg sulfate mineral found surrounding this geothermal field in this region. (B) Temperature image of the sandbar geothermal field, values are in °C.
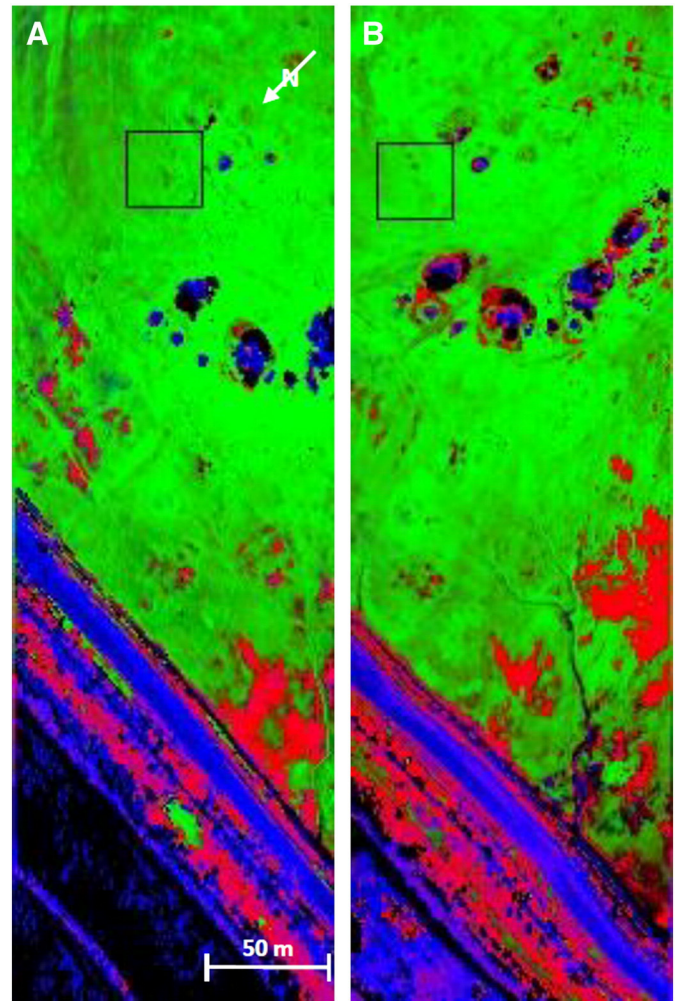
Fig. 9. Mineral maps created from the SEBASS data of the Davis–Schrimpf Geothermal field with anhydrite in red, the Mg sulfate mineral in green, and quartz in blue. The black box denotes the region of interest from which mineral percentages were extracted (Table 1). A) 26 March 2009. B) 6 April 2010.

Table 1
Mineral percentages calculated from the same region of interest in the 26 March 2009 and 6 April 2010 datasets.

Mineral percentages within same region of interest		
Mineral	March 29, 2009	April 6, 2010
Mg-sulfate	92	95
Smectite	0	0
Epsomite	0	0
Quartz	0	0
Microcline	2	0
Anhydrite	6	5
Gypsum	0	0

Differences between the 2009 and 2010 deconvolution results were also noted. Most of these were small, such as slight differences in the percentage or identification of certain end member minerals. However, a major difference was observed in the area containing the Mg-sulfate mineral. In the 2010 scene this area was three times as large (15,895 m^2 compared to 5333 m^2). This difference is likely related to the local precipitation variability in the region. Preceding the March 2009 SEBASS acquisition, there had been 2.5 to 6.4 mm of precipitation in February but no measurable rain for 36 days prior to the overflight (National Weather Service, 2011). In contrast, prior to the April 2010 acquisition, there had been 0.25 to 2.55 mm of rainfall in April and 12.7 to 25.4 mm of rainfall in March. The last measureable rainfall in the area occurred just six days prior to the SEBASS overflight (National Weather Service, 2011). The increased precipitation in 2010 could have facilitated either the leaching and later deposition of different sub-surface minerals on the surface and/or the destruction of the Mg-sulfate mineral by way of changing hydration state following the rain. Alternatively, the wetting and drying of the surface produced favorable conditions for the precipitation of these minerals from the existing soils. However, no evidence was found in the "background" soils that would indicate major changes in mineralogy or how these units would have formed from the addition of meteoric water. Regardless, it seems clear

Table 2
Deconvolution results for the mineral end members in the 26 March 2009 data extracted from the three regions of interest at each of the different spatial resolutions of the instruments. Mg sulfate mineral, epsomite, quartz, anhydrite (MEQA); Mg sulfate mineral, smectite, microcline, gypsum (MSMiG); smectite, gypsum, anhydrite, epsomite (SGAE).

2009 mineral percentage comparisons					
Minerals	SEBASS	eMAGI	eASTER (MEQA)	eASTER (MSMiG)	eASTER (SGAE)
Region 1					
Mg-sulfate	32	62	71	58	na
Smectite	2	22	na	29	58
Epsomite	15	0	22	na	1
Quartz	26	5	3	na	na
Microcline	8	10	na	12	na
Anhydrite	7	0	3	na	12
Gypsum	1	0	na	1	29
Region 2					
Mg-sulfate	98	96	98	94	na
Smectite	0	2	na	5	94
Epsomite	0	1	1	na	1
Quartz	0	0	0	na	na
Microcline	1	0	na	0	na
Anhydrite	1	1	1	na	0
Gypsum	0	0	na	1	5
Region 3					
Mg-sulfate	84	90	91	93	na
Smectite	1	1	na	1	94
Epsomite	0	0	2	na	2
Quartz	1	2	0	na	na
Microcline	2	2	na	0	na
Anhydrite	12	4	6	na	4
Gypsum	0	0	na	1	1

Table 3
Deconvolution results for the mineral end members in the 6 April 2010 data extracted from the three regions of interest at each of the different spatial resolutions of the instruments. Mg sulfate mineral, epsomite, quartz, anhydrite (MEQA); Mg sulfate mineral, smectite, microcline, gypsum (MSMiG); smectite, gypsum, anhydrite, epsomite (SGAE).

2010 mineral percentage comparisons					
Minerals	SEBASS	eMAGI	eASTER (MEQA)	eASTER (MSMiG)	eASTER (SGAE)
Region 1					
Mg-sulfate	38	50	73	76	na
Smectite	4	3	na	5	89
Epsomite	7	0	9	na	0
Quartz	12	14	4	na	na
Microcline	4	1	na	12	na
Anhydrite	28	29	14	na	9
Gypsum	4	2	na	7	1
Region 2					
Mg-sulfate	73	91	91	95	na
Smectite	0	0	na	0	93
Epsomite	0	0	0	na	0
Quartz	0	1	0	na	na
Microcline	0	0	na	1	na
Anhydrite	6	8	8	na	7
Gypsum	0	0	na	4	0
Region 3					
Mg-sulfate	73	71	81	87	na
Smectite	0	1	na	0	90
Epsomite	1	0	2	na	0
Quartz	2	2	1	na	na
Microcline	1	0	na	4	na
Anhydrite	23	26	15	na	10
Gypsum	0	0	na	8	0

that anhydrite and the spectrally-unique Mg-sulfate mineral are related both to the presence of geothermal heat and surface water in times of increased precipitation.

It is not clear whether the environmental conditions and the specific minerals identified in this study are uniquely associated with the geothermal activity at the SSGA. However, the process used to remotely identify these minerals can be quickly and easily repeated at other geothermal sites, particularly at sites with little to no surface expression of increase heat flow. Using TIR remote sensing for exploration of geothermal targets commonly relies only on identifying subtle "hot spots", which can be easily masked on the surface by solar heating and cooling by wind. For example, if a low thermal output geothermal area exists and is not detected with traditional airborne or spaceborne thermal surveys, the surface spectral signature may become far more indicative. Furthermore, areas that intermittently yield thermal anomalies could be confirmed as geothermally active target following the detection of these indicator units. If the "geothermal indicator minerals" identified here using high resolution TIR remote sensing can be classified, it is logical that geothermally-active sites elsewhere could be located using a similar approach. This would reduce the reliance on temperature, ground-based sampling, and subsequent geochemical analysis.

4.1.2. Magnesium sulfate mineral

By identifying a surface unit at the SSGA with a unique TIR spectrum in both airborne flights and laboratory data of collected samples (Fig. 4), a potentially important indicator mineral may have been found. The exact composition of this mineral (or combination of minerals) was examined using a series of geochemical and spectral analysis tools. This unit was originally located after examination of the emissivity spectrum, which has a unique and diagnostic 8.2 μm absorption feature in conjunction with a broad emissivity trough centered around 11.6 μm, which is likely produced by volume scattering of the emitted photons from fine-grained and relatively transparent particles (e.g., Salisbury and Wald, 1992). The 8.2 μm absorption band on the other hand is indicative of a primary feature resulting from bond vibration within the
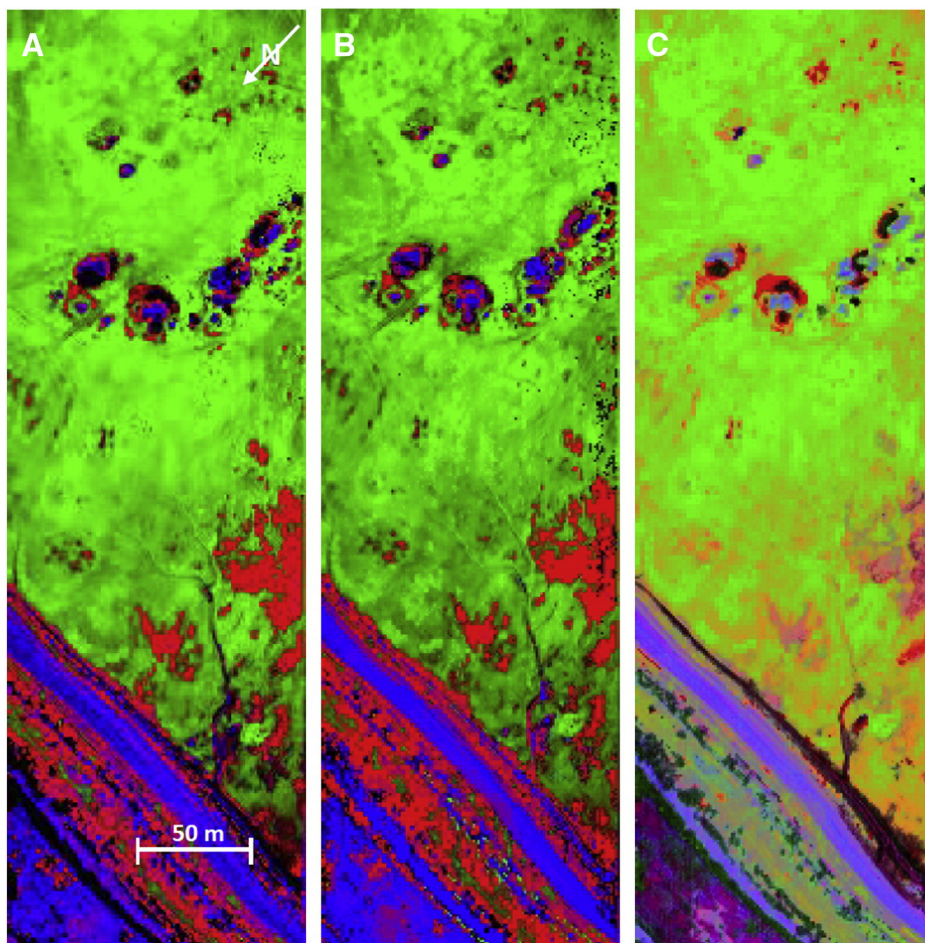
Fig. 10. Mineral maps created from the SEBASS data of the Davis–Schrimpf Geothermal field with anhydrite in red, the Mg sulfate mineral in green, and quartz in blue. These images are from the same area, at the same time, and map the same minerals. A) SEBASS, B) eMAGI, and C) eASTER.

mineral structure. Its presence was confirmed by analyzing the laboratory spectrum of a soil sample collected during the field campaign. However, some differences were noted, including a slight shift in wavelength position and the presence of a single band rather than the doublet seen in the SEBASS spectra (Fig. 4). This absorption features is similar to the ν_3 found in sulfates that range from 8.0 to 9.5 μm (Lane, 2007). However, the position of the band differs from that of other published sulfate minerals. Such a change could be attributed to a change in the hydration state of the mineral either with transport from the field or during preparation for the laboratory analysis, which requires heating for 24 hours at a temperature of 80 °C. Sulfates have a notoriously variable ν_3 which can be affected by hydration states. For example, metastable secondary sulfates like those mentioned in Hammarstrom et al. (2005) can be present in the field and later break-down during transport and changing temperature and humidity conditions. Regardless of these spectral changes, this absorption feature was identified in samples collected in March and July, although it was much more shallow in the July spectrum indicating a change in particle size as a result of transport and/or a reduction in the amount of the mineral over time (similar to the SEBASS results).

Further tests were then conducted in hopes of isolating and identifying the mineral in this sample. SEM was performed on 5 grains of the sample and a full elemental analysis of each of these grains was collected. An XRD analysis was also performed that unfortunately provided inconclusive results, finding only minerals that do not match the TIR spectra of this unit. However, during the XRD analysis two peaks at approximately 20 and 73° 2θ were found and sulfur and iron found in SEM analysis, were unaccounted. Of the grains analyzed only one contained the elements sulfur and iron; it also contained carbon, oxygen, sodium,

magnesium, aluminum, silicon, chlorine, potassium, calcium, and titanium. These elements are the same as those found in sulfate salts.

The TIR emission spectra of numerous sulfate salts were examined and some were found to have a strong TIR absorption closely resembling the unknown mineral, but at higher wavelengths. However, in theory a Mg–S pairing as well as dehydration would cause the absorption feature to move to lower wavelengths. In experiments done in Lane, 2007 the center of the ν_3 feature in $MgSO_4$ was found to vary by as much as 0.7 μm depending on hydration states. Therefore, it is believed that in order for such a low wavelength absorption feature to be present, the mineral must be some form of very to highly dehydrated magnesium sulfate. Whereas the spectrum found in the lab and remote data does not match that of a pure Mg-sulfate, the variable nature lends to addition cations (Bloedite [$Na_2Mg(SO_4)_2 \cdot 4H_2O$], Polyhalite [$K_2Ca_2Mg(SO_4)_4 \cdot 2H_2O$)], Pickeringite [$MgAl_2 (SO_4)_4 \cdot 22H_2O$]) and well as addition anions (Kainite [$KMgSO_4Cl \cdot H_2O$]) becoming incorporated into the structure. It is believed that this is the case for this mineral, however the Mg–SO_4 pairing in believed to dominate the structure, therefore it is referred to as the Mg-sulfate mineral. This conclusion is further supported based on the image compositional analysis and comparisons to the local meteorological data, the Mg-sulfate unit was determined to be water soluble enough to leach out during heavy rains and become crystalline in as few as six days of dry weather. It was found to be friable enough to erode away rather quickly, causing the reduced amounts on the surface as seen in the 2009 dataset that followed prolonged dry conditions. These facts combined with the geochemical and spectral analyses together lead to the conclusion that the unidentified mineral is likely a Mg-sulfate salt with an unknown hydration state that has yet to be fully identified using TIR spectroscopy or other geochemical techniques.

4.2. Resolution effects

The combination of spatial and spectral resolution as well as the signal-to-noise ratio of a TIR sensor will determine the absolute identification accuracy of a surface unit. Spectral resolution is perhaps the most important factor in that allows for specific absorption bands to be identified. The SEBASS sensor, with a spectral resolution of 128 TIR channels, clearly identified regions of differing surface mineralogy. The spectrally unique Mg-sulfate unit formed a distinct high concentration zone around the active geothermal vents in the Davis–Schrimpf geothermal field, causing it to be easily identified as a geothermal activity indicator. Anhydrite and gypsum, two spectrally and chemically similar minerals, with single absorption features at 8.35 to 8.65 μm in anhydrite and 8.75 μm in gypsum, were also identified in the SEBASS data. This important differentiation allows for yet another possible set of closely-related indicator minerals to be identified. The higher spatial resolution and signal-to-noise ratio of SEBASS also resulted in linear deconvolution results that were more accurate and allowed for minerals with very small areal percentages to be detected.

The simulated MAGI data, despite have four times lower spectral resolution than SEBASS, produced similar results. The Mg-sulfate unit was detected and found to form a similar pattern around the active geothermal vents. No pixels that were classified in the SEBASS analysis as containing this mineral were then excluded in the MAGI analysis, thus verifying that the MAGI sensor can successfully identify this Mg-sulfate mineral-bearing unit. Anhydrite and gypsum were also successfully differentiated at this lower spectral resolution, despite having similar spectral shapes and band positions. The MAGI sensor was eventually flown over this area in December 2011 and the preliminary analysis of the its emissivity data clearly shows surface units with distinct spectra such as gypsum, quartz, and the same Mg-sulfate surface unit (Ramsey, 2012). Although MAGI data has currently been collected, it has yet to be calibrated and processes to the detail needed for a complete scientific analysis. Comparing the unmixing percentages derived from linear deconvolution of SEBASS and eMAGI data, differences ranged from 0 to 12% with the majority of the difference occurring below 2.5%. Although there was a maximum 12% difference for the Mg-sulfate end member, the lower resolution still positively identified both the v_3 absorption feature and the volume scattering feature. Therefore, the $4\times$ lower spectral resolution of the MAGI sensor is adequate for successfully identifying potential geothermal indicator minerals to nearly the same accuracy as SEBASS data.

However, accurate mineral identification using the linear deconvolution approach became progressively worse at spectral resolutions less than 32 channels. For example, the five channel spectral resolution of the ASTER TIR sensor presented immediate shortcomings. Most notably was the fact that without at least eight channels, the full mineral suite of seven minerals could not be unmixed simultaneously. Although a direct comparison proved impossible using a step-wise deconvolution approach, the results still proved useful. Much like the case study previously performed by Hall et al. (2008) degradation to the ASTER spectral resolution resulted in a severe loss of data fidelity. Because the spectrum of the Mg-sulfate mineral is based upon a PPI spectrum it is still identified in the unmixing data. However, most of the other meaningful spectral data has been lost, such as the v_3 absorption feature and the volume scattering feature. With this evidence alone, the indicator unit could easily be missed in an actual ASTER image analysis. Anhydrite, on the other hand, was successfully identified surrounding the geothermal field. However, it was also identified in many other areas throughout the SSGA, which are agricultural fields with previously identified gypsum-rich concentrations. The differentiation between gypsum and anhydrite is therefore not possible using ASTER, and therefore anhydrite would not be useable as a geothermal indicator mineral. The differences in model results ranged from 0 to 35% with several of these occurring above 10%. Some of these differences can be expected due to the lower number of end members used, however differences as high as 35% are too large to be caused solely by this fact. These large errors are clearly due to the lack of spectral fidelity and the undersampling of potentially distinct spectral features for each mineral at the lower ASTER spectral resolution.

Data from sensors such as MAGI with spectral resolutions greater than 30 channels in the TIR wavelength region allow accurate surface unit characterization to within a few percent of laboratory data and data from sensors with hyperspectral resolution. Very few minerals have narrow spectral features in the TIR region that necessitate hyperspectral data. The efficiency of this moderate resolution data provides strong evidence that an orbital version of the sensor could identify these minerals and reduce costs by limiting excess channels, sensor mass, and ultimately cost. However, data from planned sensors such as the future HyspIRI instrument, with only a modest increase in spectral resolution in the TIR from ASTER (seven versus five), will continue to lack the ability to determine accurate surface composition of sites with geothermal potential.

5. Conclusions

Thermal infrared spectroscopy and remote sensing have been shown to be useful tools for the detection of numerous common and less common rock-forming minerals and alteration products such as those found in this study. Increased spatial and spectral resolution of the data helps to improve the accuracy of this detection as well as the increasing the number of possible mineral end members detected. SEBASS and ASTER data were used to map the surface composition surrounding the Salton Sea geothermal area (SSGA) at different spatial and spectral resolutions. The spectral resolution of the SEBASS and MAGI sensors allowed the chosen mineral end member suite to be mapped. Specific geothermal indicator minerals were identified including anhydrite and a spectrally unique mineral, which is most likely a Mg-sulfate mineral with an unknown hydration state. The proximity of these units to the active geothermal vents shows that both are related to the geothermal process in the region. The increased heat flow surrounding these vents coupled with the emplacement of water and mud are the most obvious processes leading to their presence. Identifying such specific indicator minerals could lead to the discovery of other geothermal areas using similar resolution TIR data.

The original goal of this research was to understand the accuracy of TIR remote sensing data for active geothermal exploration, focusing specifically on spectral emissivity mapping rather than detection of thermally-elevated anomalous pixels. Spaceborne sensors such as ASTER with several TIR channels allow the global land surface to be mapped, but only at level of general mineral groups rather than specific minerals. Airborne TIR sensors such as SEBASS and the more recent MAGI offer much improved spectral and spatial resolution, which will allow for specific surface minerals to be detected and quantified at geothermal areas. The four-fold reduction in spectral resolution from SEBASS to MAGI did not result in significant errors greater than that inherent in the linear deconvolution model itself. However, degrading the spectral resolution further did produce very large retrieval errors for certain minerals and lead to other surface units being missed entirely. Until spaceborne sensors are launched with at least 30 spectral channels in the TIR, detection and mapping of these specific minerals and surface units will be severely hindered.

the Planetary Science Institute about the spectral features seen in rare sulfate minerals.

References

Abrams, M., 2000. The Advanced Spaceborne Thermal Emission and Reflection Radiometer (ASTER): data products for the high spatial resolution imager on NASA's Terra platform. Int. J. Remote Sens. 21 (5), 847–859.

Adams, J.B., Smith, M.O., Johnson, P.E., 1986. Spectral mixture modeling: a new analysis of rock and soil types at the Viking Lander 1 site. J. Geophys. Res. 91 (B8), 8098–8112.

Adams, J.B., Smith, M.O., Gillespie, A.R., 1989. Simple models for complex natural surfaces: a strategy for the hyperspectral era of remote sensing. Proc. IGARSS Can. Symp. Remote Sens., 12th, pp. 16–21.

Azimi, G., Papangelakis, V.G., 2010. The solubility of gypsum and anhydrite in simulated laterite pressure acid leach solutions up to 250 ° C. Hydrometallurgy 102 (1), 1–13.

Baldridge, A.M., Hook, S.J., Grove, C.I., Rivera, G., 2009. The ASTER spectral library version 2.0. Remote Sens. Environ. 113, 711–715.

Buck, B.J., King, J., Etyemezian, V., 2011. Effects of salt mineralogy on dust emissions, Salton Sea, California. Soil Sci. Soc. Am. J. 75 (5), 1971–1985.

Christensen, P.R., Bandfield, J.L., Hamilton, V.E., Howard, D.A., Lane, M.D., Piatek, J.L., Ruff, S.W., Stefanov, W.L., 2000. A thermal emission spectral library of rock-forming minerals. J. Geophys. 9735–9739.

Crowley, J.K., Hook, S.J., 1996. Mapping playa evaporite minerals and associated sediments in Death Valley, California, with multispectral thermal infrared images. J. Geophys. Res. Solid Earth (1978–2012) 101 (B1), 643–660.

Dean, K.G., Dehn, J., Papp, K.R., Smith, S., Izbekov, P., Peterson, R., Steffke, A., 2004. Integrated satellite observations of the 2001 eruption of Mt. Cleveland, Alaska. J. Volcanol. Geotherm. Res. 135 (1), 51–73.

Elders, W.A., Sass, J.H., 1988. An Overview of the Salton Sea Drilling Project, JGR November 10.

Elders, W.A., Biehler, S., Rex, R.W., Robinson, P.T., Meidav, T., 1972. Crustal spreading in Southern California: the Imperial Valley and the Gulf of California formed by the rifting apart of a continental plate. Science 178, 15–24. http://dx.doi.org/10.1126/science.178.4056.15.

Gillespie, A.R., 1985. Lithologic mapping of silicate rocks using TIMS. The TIMSData User's Workshop, June 18–19, 1985, JPL Pub. 86-38, pp. 29–44.

Gillespie, A.R., 1992a. Enhancement of multispectral thermal infrared images: decorrelation contrast stretching. Remote Sens. Environ. 42, 147–155.

Gillespie, A.R., 1992b. Spectral mixture analysis of multispectral thermal infrared images. Remote Sens. Environ. 42 (2), 137–145.

Gillespie, A.R., Kahle, A.B., Palluconi, F.D., 1984. Mapping alluvial fans in Death Valley, CA, using multispectral thermal infrared images. Geophys. Res. Lett. 11 (11), 1153–1156.

Gillespie, A.R., Kahle, A.B., Walker, R.E., 1986. Color enhancement of highly correlated images: I. Decorrelation and HIS contrast stretches. Remote Sens. Environ. 20, 209–235.

Hackwell, J.A., Warren, D.W., Bongiovi, R.P., Hansel, S.J., Hayhurst, T.L., Mabry, D.J., Sivjee, M.G., Skinner, J.W., 1996. LWIR/MWIR imaging hyperspectral sensor for airborne and ground-based remote sensing. Proc. SPIE 2819, 102–107.

Hall, J.L., Hackwell, J.A., Tratt, D.M., Warren, D.W., Young, S.J., 2008. Space-based mineral and gas identification using a high-performance thermal infrared imaging spectrometer. Proc. SPIE 7082, 70820M.

Hammarstrom, J.M., Seal II, R.R., Meier, A.L., Kornfeld, J.M., 2005. Secondary sulfate minerals associated with acid drainage in the eastern US: recycling of metals and acidity in surficial environments. Chem. Geol. 215 (1), 407–431.

Helgeson, H.C., 1968. Geologic and thermodynamic characteristics of the Salton Sea geothermal system. Am. J. Sci. 266, 129–166 (March).

Herzig, C.T., Mehegan, J.M., Stelting, C.E., 1988. Lithostratigraphy of the State 2–14 borehole: Salton Sea scientific drilling project. Journal of Geophysical Research 93 (B11) 12969-12912.

Hook, S.J., Abbott, E.A., Grove, C., Kahle, A.B., Palluconi, F.D., 1999. Use of multispectral thermal infrared data in geological studies, In: Rencz, A.N. (Ed.), 3rd ed. Remote Sensing for the Earth Sciences: Manual of Remote Sensing, vol. 3. Wiley, New York, pp. 59–110.

Hook, S.J., Myers, J., Thome, K.J., Fitzgerald, M., Kahle, A.B., 2001. The MODIS/ASTER airborne simulator (MASTER) — a new instrument for earth science studies. Remote Sens. Environ. 76, 93–102.

Ives, R.L., 1951. Mud volcanoes of the Salton depression. Rocks Miner 26, 227–235.

Johnson, B.R., Young, S.J., 1998. In-Scene Atmospheric Compensation: Application to SEBASS Data Collected at the ARM Site. Technical Report, Space and Environment Technology Center, The Aerospace Corporation, May.

Jordan, G., Astilleros, J.M., 2006. In situ HAFM study of the thermal dehydration on gypsum (010) surfaces. Am. Mineral. 91 (4), 619–627.

Kahle, A.B., Rowan, L.C., 1980. Evaluation of multispectral middle infrared aircraft images for lithologic mapping in the East Tintic Mountains, Utah. Geology 8, 234–239.

King, P.L., Ramsey, M.S., McMillan, P.F., Swayze, G., 2004. Laboratory Fourier transform infrared spectroscopy methods for geologic samples. In: King, P.L., Ramsey, M.S., Swayze, G.A. (Eds.), Infrared Spectroscopy in Geochemistry, Exploration Geochemistry,

and Remote Sensing, 33. Mineralogical Association of Canada, London, Ontario, pp. 57–91.

King, J., Etyemezian, V., Sweeney, M., Buck, B.J., Nikolich, G., 2011. Dust emission variability at the Salton Sea, California, USA. Aeolian Res. 3 (1), 67–79.

Lane, M.D., 2007. Mid-infrared emission spectroscopy of sulfate and sulfate-bearing minerals. Am. Mineral. 92 (1), 1–18.

Lynch, D.K., Hudnut, K.W., Adams, P.M., 2013. Development and growth of recently-exposed fumarole fields near Mullet Island, Imperial County, California. Geomorphology 193, 27–44.

MacDonald, G.J.F., 1953. Anhydrite–gypsum equilibrium relations. Am. J. Sci. 251, 884–898.

National Weather Service, 2011. Advanced Hydrologic Prediction Service, Precipitation. water.weather.gov/precip/ (May 12, 2001).

Onderdonk, N., Mazzini, A., Shafer, L., Svensen, H., 2011. Controls on the geomorphic expression and evolution of gryphons, pools, and caldera features at hydrothermal seeps in the Salton Sea Geothermal Field, southern California. Geomorphology 130 (3), 327–342.

Prata, A.J., Grant, I.F., 2001. Determination of mass loadings and plume heights of volcanic ash clouds from satellite data. CSIRO Atmospheric Research Technical Paper, 48 (41 pp.).

Ramsey, M.S., 2012. Implications of temporal and spectral resolution changes for HyspIRI TIR data of volcanoes, 2012 HyspIRI Science Workshop, Washington, DC.

Ramsey, M.S., Christensen, P.R., 1998. Mineral abundance determination: quantitative deconvolution of thermal emission spectra. JGR 103 (B1), 577–596.

Realmuto, V.J., 1990. Separating the effects of temperature and emissivity: emissivity spectrum normalization. Proceedings of the 2nd TIMS Workshop, 2, pp. 31–35.

Rowan, L.C., Mars, J.C., Simpson, C.J., 2005. Lithologic mapping of the Mordor, NT, Australia ultramafic complex by using the Advanced Spaceborne Thermal Emission and Reflection Radiometer (ASTER). Remote Sens. Environ. 99 (1), 105–126.

Ruff, S.W., Christensen, P.R., Barbera, P.W., Anderson, D.L., 1997. Quantitative thermal emission spectroscopy of minerals: a laboratory technique for measurement and calibration. J. Geophys. Res. All Ser. 102, 14.

Sabine, C., Realmuto, V.J., Taranik, J.V., 1994. Quantitative estimation of granitoid composition from thermal infrared multispectral scanner (TIMS) data, desolation wilderness, Northern Sierra Nevada, California. J. Geophys. Res. 99 (B3), 4261–4271.

Salisbury, J.W., Wald, A., 1992. The role of volume scattering in reducing spectral contrast of reststrahlen bands in spectra of powdered minerals. Icarus 96, 121–128.

Salisbury, J.W., Wald, A., D'Aria, D.M., 1994. Thermal-infrared remote sensing and Kirchhoff's law: 1. Laboratory measurements. J. Geophys. Res. Solid Earth (1978–2012) 99 (B6), 11897–11911.

Short, N.M., Stuart, L.M., 1983. The heat capacity mapping mission (HCMM) anthology. NASA SP, vol. 465. US Government Printing Office, Washington, DC.

Spencer, R.J., 2000. Sulfate minerals in evaporite deposits, in sulfate minerals: crystallography, geochemistry, and environmental significance. Rev. Mineral. Geochem. 40.

Sturz, A.A., Kamps, R.L., Earley, P.J., 1992. Temporal changes in mud volcanos, Salton Sea geothermal area. Water-Rock Interact. 2, 1363–1366.

Svensen, H., Karlsen, D.A., Sturz, A., Backer-Owe, K., Banks, D.A., Planke, S., 2007. Processes controlling water and hydrocarbon composition in seeps from the Salton Sea geothermal system, California, USA. Geology 35 (1), 85–88.

Svensen, H., Hammer, Ø., Mazzini, A., Onderdonk, N., Polteau, S., Planke, S., Podladchikov, Y., 2009. Dynamics of hydrothermal seeps from the Salton Sea Geothermal System (California, USA) constrained by temperature monitoring and time series analysis. J. Geophys. Res. B09201. http://dx.doi.org/10.1029/2008JB00624.

Sweeney, M.R., McDonald, E.V., Etyemezian, V., 2011. Quantifying dust emissions from desert landforms, eastern Mojave Desert, USA. Geomorphology 135 (1), 21–34.

Taranik, J.V., 1988. Application of aerospace remote sensing technology to exploration for precious metal deposits in the western United States. In: Schafer, R.W. (Ed.), Bulk Mineable Precious Metal Deposits of the Western United States, GSN Symposium Proceedings. Geological Society of Nevada, Reno, NV, pp. 551–575.

Thome, K., Palluconi, F., Takashima, T., Masuda, K., 1998. Atmospheric correction of ASTER. IEEE Trans. Geosci. Remote Sens. 36 (4), 1199–1211.

Thompson, J.M., Fournier, R.O., 1988. Chemistry and geothermometry of brine produced from the Salton Sea scientific drill hole, Imperial Valley, California. J. Geophys. Res. 93, 13,165–13,173.

Van de Kamp, P.C., 1973. Holocene continental sedimentation in the Salton Basin, California: a reconnaissance. Geol. Soc. Am. Bull. 84, 827–848.

Vaughan, R.G., Calvin, W.M., Taranik, J.V., 2003. SEBASS hyperspectral thermal infrared data: surface emissivity measurement and mineral mapping. Remote Sens. Environ. 85, 48–63.

Wolf, E., Born, M., 1965. Principles of Optics. Pergamon Press.

Wright, R., Flynn, L., Garbeil, H., Harris, A., Pilger, E., 2002. Automated volcanic eruption detection using MODIS. Remote Sens. Environ. 82 (1), 135–155.

Younker, L.W., Kasameyer, P.W., Tewhey, J.D., 1982. Geological, geophysical, and thermal characteristics of the Salton Sea Geothermal Field, California. J. Volcanol. Geoth. Res. 12 (3–4), 221–258.

Zhang, X., Pazner, M., Duke, N., 2007. Lithologic and mineral information extraction for gold exploration using ASTER data in the south Chocolate Mountains (California). ISPRS J. Photogramm. Remote Sens. 62 (4), 271–282.